

Article

Comparison of the Effects of Ultrasonic and Ball Milling on Red Mud Desulfurization

Xueke Li, Yan Liu *  and Tingan Zhang

Key Laboratory of Ecological Metallurgy of Multi-Metal Intergrown Ores of Ministry of Education, School of Metallurgy, Northeastern University, Shenyang 110819, China

* Correspondence: liuyan@smm.neu.edu.cn

Abstract: Red mud desulfurization is an environmentally friendly desulfurization technology. After desulfurization, the acidity of red mud slurry continues to be neutralized for processing new red mud, and no waste acid is generated. At present, there is a lack of research on desulfurization intensification in external fields, etc. To further enhance red mud desulfurization, this paper used an SO₂ detector, X-ray fluorescence spectrometer (XRF), and scanning electron microscope (SEM) to compare and analyze red mud desulfurization under the action of ball mill and ultrasonic external fields. In this study, experiments were conducted using a bubbling and stirring reactor device. The results showed that the suitable red mud slurry concentration was 10 g/L. The raw red mud desulfurization (without external field condition) could reach 100% absorption in the first 25 min, and the desulfurization rate dropped to 81.3% at 80 min. The mechanism of red mud desulfurization was investigated by X-ray diffractometer (XRD), XRF, and infrared spectroscopy. Under the action of the external field of the ball mill, the red mud particles could be refined to prolong the desulfurization time. The red mud after ball milling could reach 100% absorption within 33 min. Under the thermal effect of the ultrasound, 100% absorption could only be achieved within 23 min. From the desulfurization effect and XRF results, it was found that the ball mill was more suitable for promoting red mud desulfurization in the bubbling and stirring reactor.



Citation: Li, X.; Liu, Y.; Zhang, T. Comparison of the Effects of Ultrasonic and Ball Milling on Red Mud Desulfurization. *Metals* **2022**, *12*, 1887. <https://doi.org/10.3390/met12111887>

Academic Editor: Petros E. Tsakiridis

Received: 8 October 2022

Accepted: 1 November 2022

Published: 4 November 2022

Publisher's Note: MDPI stays neutral with regard to jurisdictional claims in published maps and institutional affiliations.



Copyright: © 2022 by the authors. Licensee MDPI, Basel, Switzerland. This article is an open access article distributed under the terms and conditions of the Creative Commons Attribution (CC BY) license (<https://creativecommons.org/licenses/by/4.0/>).

Keywords: ball mill machinery outfield; desulfurization; desulfurization mechanism; red mud; ultrasonic outfield

1. Introduction

Red mud is an alkaline solid waste produced in the process of producing alumina from bauxite [1]. For every 1 ton of alumina produced, 1–2 tons of red mud are generated [2,3]. Approximately 120 million tons of red mud are produced annually [4]. Currently, most of the red mud is disposed of by stockpiling. Long-term storage of highly alkaline red mud will not only waste land resources but also cause environmental pollution [5,6].

The composition of red mud varies depending on the way in which alumina is produced. Red mud generally includes Al₂O₃, CaO, SiO₂, Fe₂O₃, Na₂O, and other chemical components. According to the characteristics of red mud, it is of great significance to reasonably treat and reuse red mud resources. Red mud has a high surface reactivity, a large specific surface area, and a porous structure that allows it to adsorb harmful metals, phosphates, and other inorganic salts and organic matter from aqueous solutions [7–9]. Red mud contains a large amount of Al, Fe, Ti, Na, and other metal elements, and valuable metal elements in red mud can be recovered [10,11]. The residual iron oxide, quartz, and sodium silica-aluminate in red mud can be used as additives to condition and improve soil [12–15]. Red mud is used to construct ceramics [16], ceramic glazes [17], bricks, roof tiles [18,19], cement [20], geopolymers [21], and other building materials. The characteristics of red mud, such as strong alkalinity, fine particles, and large specific surface area, allow for mineralized sequestration of CO₂ [22]. Red mud can also be used to absorb and treat acidic waste gases, such as nitrides [23,24], H₂S [25], SO₂, fluoride [26], etc.

SO₂, as an irritant gas, is harmful to the human body and the environment. Flue gas desulfurization technologies are dry desulfurization, semidry desulfurization, and wet desulfurization. Red mud for desulfurization is solid waste reused to purify flue gas. Red mud desulfurization is also a way to solve red mud stockpiles. Red mud can be used for dry adsorption desulfurization. At present, research on the dry desulfurization of red mud is shown as follows. Yan et al. [27] used red mud instead of CaO for desulfurization in a circulating fluidized bed with the highest desulfurization rate of more than 94%. Liu et al. [28] used red mud-modified limestone for desulfurization by adsorption in a tube furnace. Niu et al. [29] used red mud as an additive to activated carbon to improve the desulfurization capacity of activated carbon, and the maximum sulfur capacity was increased by 17.9% compared with activated carbon alone. Red mud is highly alkaline, and the slurry made from red mud for desulfurization is a wet desulfurization process. There is a lot of work carried out in the field of red mud slurry for wet desulfurization. Wang et al. [30] studied the effect of red mud slurry desulfurization and decarbonization on red mud dealkalization. The main components of red mud residue after desulfurization and decarbonization are SiO₂, Fe₂O₃, and AlOOH. Wei [31] obtained the optimal operating conditions for desulfurization of an absorption tower with red mud slurry in an absorption tower. The desulfurization rate was above 95%, and the red mud slurry lost its desulfurization capacity after 10 h. Yang [32] performed red mud slurry desulfurization in a desulfurization absorption tower and obtained the optimum operating conditions with a maximum desulfurization rate of 98.8%. Li et al. [33] used ozone peroxidation of red mud slurry desulfurization and denitrification in a spray absorption tower, and the desulfurization rate was stabilized at 98% within 1 h. The reaction mechanism of desulfurization and denitrification was investigated. Tao et al. [34] used red mud slurry desulfurization in a bubbling reactor and found that the liquid/solid ratio had the most significant effect on the desulfurization process. Liu et al. [35] used a yellow phosphorus emulsion coupled with red mud for desulfurization and denitrification to optimize the reaction conditions. Under the optimized conditions, the optimal desulfurization and denitrification rates were as high as 97.9% and 100%, respectively. Zhang et al. [36] established an industrial demonstration of red mud-limestone with a desulfurization rate of 98.9%, which can meet ultralow emissions requirements.

In this paper, a large number of studies on wet desulfurization of red mud slurry were investigated using a bubbling and stirring reactor. In addition, the mechanism of red mud desulfurization was discussed in relation to XRD, XRF, and infrared spectroscopy. Red mud slurry desulfurization could make the Na₂O content in red mud lower than 1% and realize the reduction of red mud alkalinity, thus making red mud more effective for the production of cement, geopolymers, etc. The existing studies on red mud desulfurization concern the process of desulfurization, and there are fewer studies on red mud desulfurization under the action of external field intensification. Mechanical energy can initiate and promote chemical reactions. The mechanical ball milling method can easily induce chemical reactions by reducing the reaction activation energy through shear, abrasion, impact, extrusion, and other mechanical force effects. When an ultrasound propagates in the gas-liquid-solid phase, it produces cavitation phenomena and is accompanied by mechanical, thermal, chemical, and biological effects. Therefore, to better enhance the promotion of red mud slurry desulfurization, the external field of the mechanical energy of the ball mill and the external field of the ultrasonic mechanical wave were used in this paper. The effect of two external fields on the desulfurization of red mud slurry was investigated.

2. Experimental Section

2.1. Experimental Procedures

In this study, the red mud slurry desulfurization reaction was carried out in a bubbling and stirring reactor (Tianjin Tianke Glass Instrument Manufacturing Co., Tianjin, China) at room temperature. The experimental setup is shown in Figure 1. It mainly includes a gas supply device, absorption device, and analysis device. The specific experimental

process is as follows: SO_2 gas is supplied by a compressed stainless steel bottle, controlled by a gas flow meter, and the SO_2 inlet flow rate is 400 mL/min. SO_2 is refined by aeration stones, and bubbles escape at the bottom of the reactor to react with the red mud slurry. The stirring paddle in the reactor continuously disperses the red mud and renews the absorption reaction interface. The speed of the stirring paddle was controlled at 350 r/min. The pH change of the slurry was measured by a Thunder Magnetic pH Meter (PHSJ-3F, Shanghai Jingke Company, Shanghai, China) during the absorption reaction. SO_2 gas after the reaction was measured by an SO_2 detector (Leibo 3040, Jiangsu Leibo Scientific Instruments Co., Jiangyin, China) for concentration. The unreacted SO_2 tail gas is passed into the NaOH solution. The desulfurized red mud residue was filtered and dried for characterization and determination.

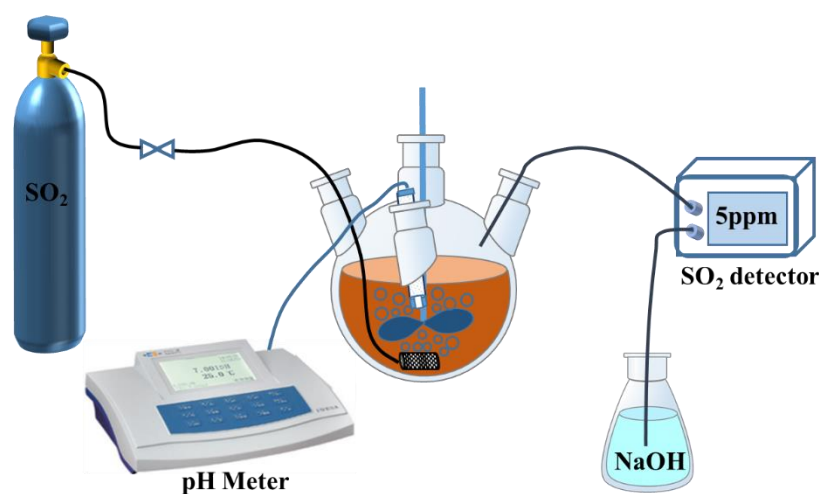


Figure 1. Experimental setup diagram.

The absorption reactor was a 1 L four-neck flask with a red mud slurry volume of 700 mL. The red mud is mechanically refined by a planetary high-energy ball mill (Fritz Instrument Equipment Co., Hamburg, Germany) to refine the particles. The ball milling speed was 300 r/min, and the ball milling time was 1 h. The ultrasonic mechanical wave for the reaction process was provided by a 40 kHz ultrasonic cleaner (CJ-060B, Shenzhen Super Clean Technology Industrial Co., Shenzhen, China). Figure 2 illustrates the two modes of action of red mud desulfurization performed under external fields.

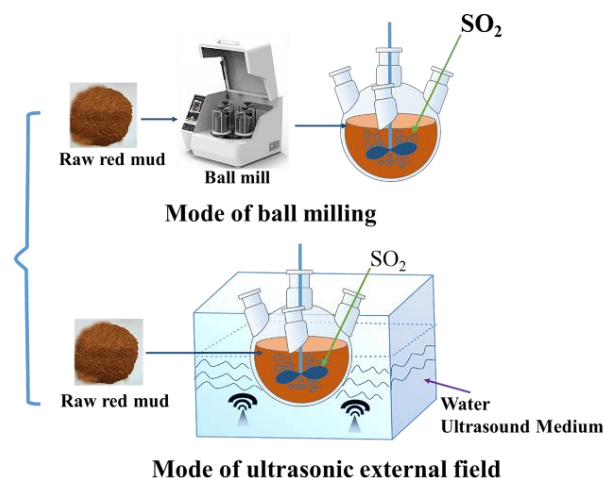


Figure 2. The two modes of action of the external field.

There are also some test devices as follows: X-ray fluorescence spectrometer (XRF, ZSXPrimus, Hitachi Co., Tokyo, Japan) was used to detect the component content of the phase; the specific surface area physical adsorption analyzer (ASAP2020, American Micromachined Instruments, Atlanta, GA, USA) was used to analyze the pore structure of the phase; X-ray diffractometer (XRD, Bruker Co., Karlsruhe, Germany) was used to determine the phase composition; field emission scanning electron microscope (SEM, Zeiss Sigma 300, Carl Zeiss AG, Oberkochen, Germany) was used to detect the phase micromorphology; Fourier transform infrared spectrometer (Nicolet IS 50, Thermo Fisher, Waltham, MA, USA) was used to measure the change in the mid-infrared absorption peak.

2.2. Experimental Materials

The concentration of SO_2 gas used in the experiment was 5000 ppm, balanced with N_2 (Shenyang Shuntai Special Gas Co., Shenyang, China). The red mud used in the experiment came from an aluminum factory in Shanxi, China. The ingredients of the raw materials are listed in Table 1. To better promote the absorption of SO_2 in red mud, the red mud particles were broken by mechanical ball milling. The absorption reaction rate can be improved by refining the particles and increasing the specific surface area of the particles from a macroscopic point of view. The adsorption–desorption isotherms before and after ball milling are shown in Figure 3. The curves of the red mud samples before and after ball milling showed a typical type IV adsorption–desorption isothermal curve. According to the adsorption–desorption isotherm, the specific surface area of the raw red mud is $98.35 \text{ m}^2/\text{g}$, and the specific surface area after ball milling is $32.46 \text{ m}^2/\text{g}$, as defined by the Brunauer–Emmett–Teller (BET) gas adsorption method [37]. The red mud is dried and filtered through an 80 mesh sieve before being added to the reactor.

Table 1. Compositions of raw red mud (wt.%).

Sample	Al_2O_3	SiO_2	Fe_2O_3	TiO_2	Na_2O	CaO	SO_3
Raw red mud	17.78	11.88	39.82	6.93	5.94	2.38	0.48

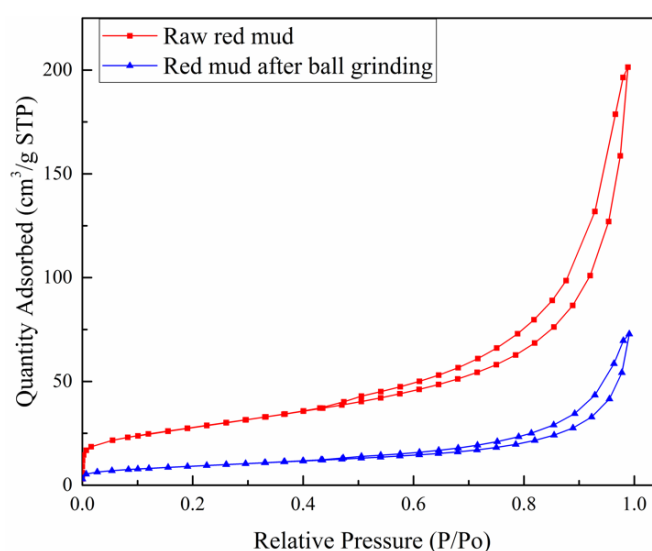


Figure 3. Adsorption–desorption isotherms before and after ball milling.

From Figure 4, it can be seen that the original red mud is formed by cohesions, agglomerates, and agglomerates to form a loose structure. There are spherical particles attached to the surface. In addition, some particles have agglomeration behavior. The microscopic morphology of the red mud after ball milling is not significantly changed. Combined with Figure 3, it can be seen that the collision of steel balls in the ball mill can

transfer more mechanical energy to the particles, thus changing the specific surface area of the red mud particles.

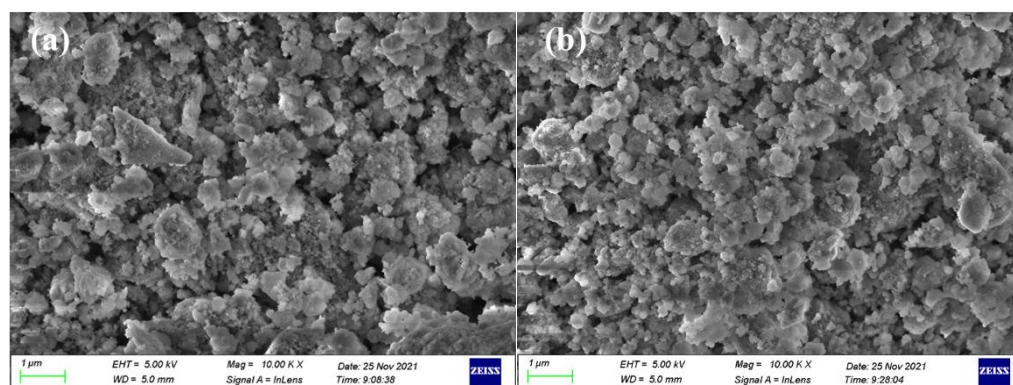


Figure 4. 10 K magnification SEM images of (a) raw red mud; (b) red mud after ball milling.

2.3. Calculation of Desulfurization Rate

The experimental parameter of the desulfurization rate can better reflect the desulfurization efficiency of red mud. The equation of desulfurization rate is shown in Equation (1).

$$\text{Desulfurization rate} = \frac{C_{\text{inlet}} - C_{\text{outlet}}}{C_{\text{inlet}}} \times 100\% \quad (1)$$

where C_{inlet} is the SO_2 concentration at the reactor inlet, ppm; C_{outlet} is the SO_2 concentration in the tail gas at the reactor outlet, ppm.

3. Results and Discussion

3.1. The Effect of Red Mud Slurry Concentration on Desulfurization

From the study of Tao et al. [34], we know that the liquid–solid ratio has the most significant effect on the desulfurization of red mud. Therefore, this paper focuses on the effect of slurry concentration on desulfurization, which is used to select the optimal slurry concentration. The influence of slurry concentration on the desulfurization process was characterized by the change in slurry pH value. As shown in Figure 5, in the red mud slurry desulfurization process, the pH value changes over time into three stages: a rapid decline stage, a slow decline stage, and an unchanged stage. When the concentration of red mud slurry increases from 7 g/L to 10 g/L, the time of pH drop is prolonged. This means that an increase in concentration can prolong the absorption reaction time and absorb and process more SO_2 . When the slurry concentration of red mud increases from 10 g/L to 15 g/L, the increase in slurry concentration does not prolong the absorption reaction time in the first 10 min. With the increase in slurry concentration, the free alkali in red mud and other substances that react with SO_2 cannot be dissolved in a short time. With increasing time, 15 g/L red mud can have a longer absorption reaction time. However, as its absorption reaction time is not much different from that of 10 g/L red mud, the red mud slurry concentration is selected as 10 g/L in the following experiments after comprehensive consideration. In addition, the slurry after desulfurization can neutralize the new red mud and no waste acid is generated.

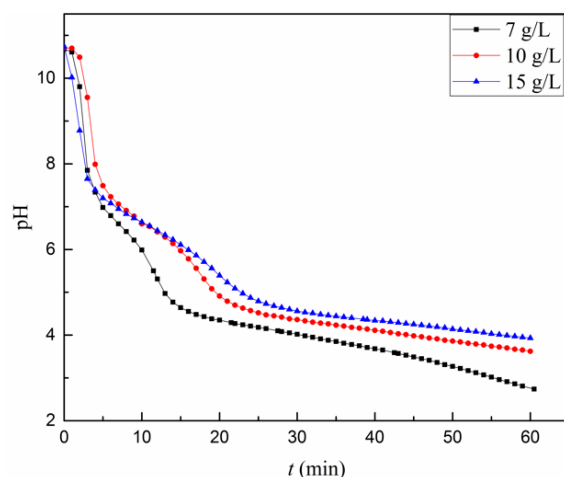


Figure 5. Changes in pH with red mud slurry concentration.

3.2. The Effect of Red Mud Slurry Concentration on Desulfurization

3.2.1. Changes in Slurry pH and Desulfurization Efficiency during Red Mud Desulfurization

As shown in Figure 6, the changing trend of the red mud after ball milling is the same as that of the raw red mud. The raw red mud (without external field conditions) can completely absorb low-concentration SO_2 in the first 25 min, and the desulfurization rate is maintained at 100%. After 25 min, the absorption of SO_2 in red mud gradually reaches saturation, and the concentration of SO_2 in tail gas increases continuously. The red mud desulfurization rate drops to 81.3% after 80 min. After ball milling, red mud desulfurization uses mechanical energy to refine the red mud particles, promote the decomposition of the red mud particles, and prolong the desulfurization time. It can completely absorb low concentrations of SO_2 in the first 33 min, and the desulfurization rate is maintained at 100%. After 33 min, the absorption capacity of SO_2 decreases gradually, and the concentration of SO_2 in the tail gas increases continuously. The desulfurization rate of red mud after ball milling is still at 88.2% at 80 min.

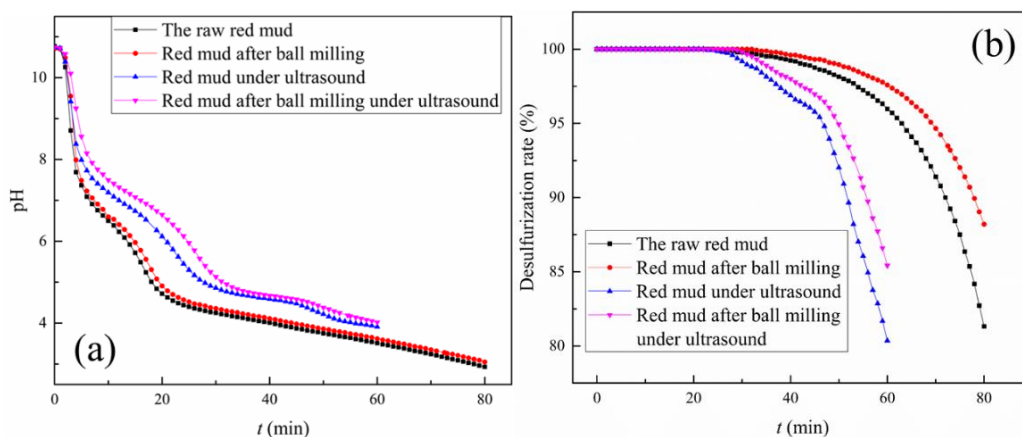


Figure 6. (a) Variation of slurry pH; (b) variation of desulfurization rate.

As a kind of high-frequency mechanical wave, an ultrasound provides a cavitation effect, thermal effect, and mechanical effect, and a study on the effect of an ultrasonic external field on red mud desulfurization was conducted. Under the effect of an ultrasonic field, the desulfurization rate of raw red mud reaches 100% in the first 23 min, and the desulfurization ability gradually decreases after 23 min. The desulfurization rate drops to 80.4% at 60 min. Compared to desulfurization without ultrasound that can absorb 100%

in the first 25 min, ultrasound instead reduces the slurry desulfurization time. Under the action of an ultrasonic field, the desulfurization rate of ball-milled red mud is 100% in the first 29 min, and the desulfurization capacity decreases gradually after 29 min. Then, the desulfurization rate drops to 85.4% at 60 min. The SO_2 in the exhaust gas is detected earlier in the presence of an ultrasonic field, considering that the thermal effect of ultrasound increases the temperature of the slurry, and the temperature affects the solubility of SO_2 . Therefore, through the above study, it is found that in the bubble stirred reactor, the thermal effect of ultrasonic waves would reduce the solubility of SO_2 in the slurry by increasing the slurry temperature, leading to a decrease in the desulfurization rate. Furthermore, the ball mill outfield can make the slurry have a longer absorption time and improve the desulfurization capacity of red mud by refining the red mud particles. In the practical application of red mud desulfurization, the ball mill can be selected to refine the particles to extend the desulfurization time.

According to the air pollutant emission standards in various parts of China, the desulfurization rate should be at least 90%. In this paper, the amount of red mud slurry required to absorb 1 kg of SO_2 under the influence of external field is calculated based on the absorption time for a desulfurization rate of 90%. The calculation results are shown in Table 2.

Table 2. The amount of red mud slurry required to absorb 1 kg of SO_2 .

Desulfurization Method	Desulfurization Time (min)	The Amount of Red Mud Slurry (kg/m^3)
Raw red mud	72	24.3
Red mud after ball milling	77	22.7
Red mud under ultrasound	52	33.7
Red mud after ball milling under ultrasound	55	31.8

3.2.2. Changes in Red Mud Composition during Red Mud Desulfurization

XRF was used to detect the composition changes of red mud in the desulfurization process under various conditions, and the detection results are shown in Table 3.

Table 3. XRF results of the compositions of red mud in the desulfurization process (wt.%) (raw red mud desulfurization (RR), ball mill red mud desulfurization (BR), raw red mud desulfurization under an ultrasonic external field (RU), ball mill red mud desulfurization under ultrasonic external field (BU)).

Samples	Al_2O_3	SiO_2	Fe_2O_3	TiO_2	Na_2O	CaO	SO_3
RR t = 20 min	19.24	12.23	42.13	7.39	5.02	0.69	0.82
RR t = 40 min	18.89	6.41	47.94	8.58	1.07	0.11	2.32
RR t = 60 min	16.63	4.91	52.73	9.53	0.8	0.07	1.55
RR t = 80 min	14.44	3.75	55.25	10.31	0.45	-	1.01
BR t = 20 min	19.33	12.72	42.08	7.63	4.02	0.36	0.9
BR t = 40 min	18.03	4.6	49.98	9.25	0.42	-	2.24
BR t = 60 min	14.95	3.66	54.77	10.45	0.4	-	1.49
BR t = 80 min	13.56	3.31	56.42	10.94	0.39	-	0.97
RU t = 20 min	19.76	12.29	41.5	7.34	4.29	0.57	0.86
RU t = 40 min	21.12	7.26	43.89	7.66	1.16	-	3.2
RU t = 60 min	16.95	4.41	52.25	9.43	0.41	-	1.54
BU t = 20 min	19.56	12.71	40.94	7.32	4.27	0.75	0.91
BU t = 40 min	20.76	8.11	43.6	7.78	1.19	-	2.58
BU t = 60 min	17.42	5.19	47.27	8.71	0.41	-	3.14

From the XRF results of red mud in the desulfurization process in Tables 1 and 2, it is clear that Al and Na are more easily dissolved in the initial stage of the reaction. As the desulfurization reaction proceeds, the slurry becomes more acidic, and the aluminum and silicon in the red mud begin to dissolve in large amounts [38]. The iron minerals are relatively stable, and the Fe_2O_3 content is almost unaffected by the desulfurization reaction. With the continuous dissolution of Na, Al, and Si, the mass of red mud decreases, which is also the reason for the increase in Fe_2O_3 content. CaO and TiO_2 were partially dissolved with the reaction. The dissolution rate of Ti and Ca metal substances increased with the intensification of ultrasonication [39]. The Na_2O content in the red mud of the desulfurization process in Table 2 is represented in Figure 7. Figure 7 clearly shows the decreasing content of Na_2O in the red mud as desulfurization proceeds. The Na_2O content in red mud is further reduced by the action of ball milling and ultrasonic external fields. This shows that the external field is more conducive to red mud dealkalization. For the red mud after 60 min of desulfurization under the above conditions, the content of Na_2O is $<1\%$, which can meet the composition requirements of cement, brick, geopolymers, and other construction materials [40]. The S content in the desulfurized red mud did not increase significantly, indicating that the red mud is mainly dissolved in the liquid phase.

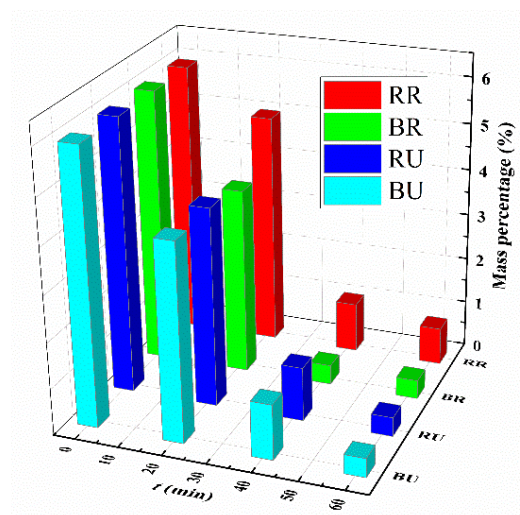


Figure 7. Changes in Na_2O content in red mud during desulfurization (raw red mud desulfurization (RR), ball mill red mud desulfurization (BR), raw red mud desulfurization under an ultrasonic external field (RU), ball mill red mud desulfurization under ultrasonic external field (BU)).

3.2.3. Changes in Red Mud Composition during Red Mud Desulfurization

Figure 8 shows the SEM image of the red mud with a desulfurization time of $t = 60$ min. Compared with the undesulfurized SEM image in Figure 4, the microscopic morphology of the red mud changed significantly after desulfurization. In red mud desulfurization, the solid phase material in the red mud is involved in the reaction, where it is continuously consumed. After desulfurization, the red mud is broken down into many small spherical particles, and the microstructure of the red mud becomes loose as a result. The microstructure of red mud is more fluffy after desulfurization by ball milling. The ultrasonically dispersed particles are more uniform, and the desulfurized red mud has more small spherical particles and smaller pores. In conclusion, the change of desulfurization rate shows that the mechanical external field of the ball mill can extend the desulfurization time by refining the red mud particles. The ultrasonic external field disperses the red mud particles, and the XRF results show that the dispersed red mud particles promote the dissolution of metals such as Ti and Ca.

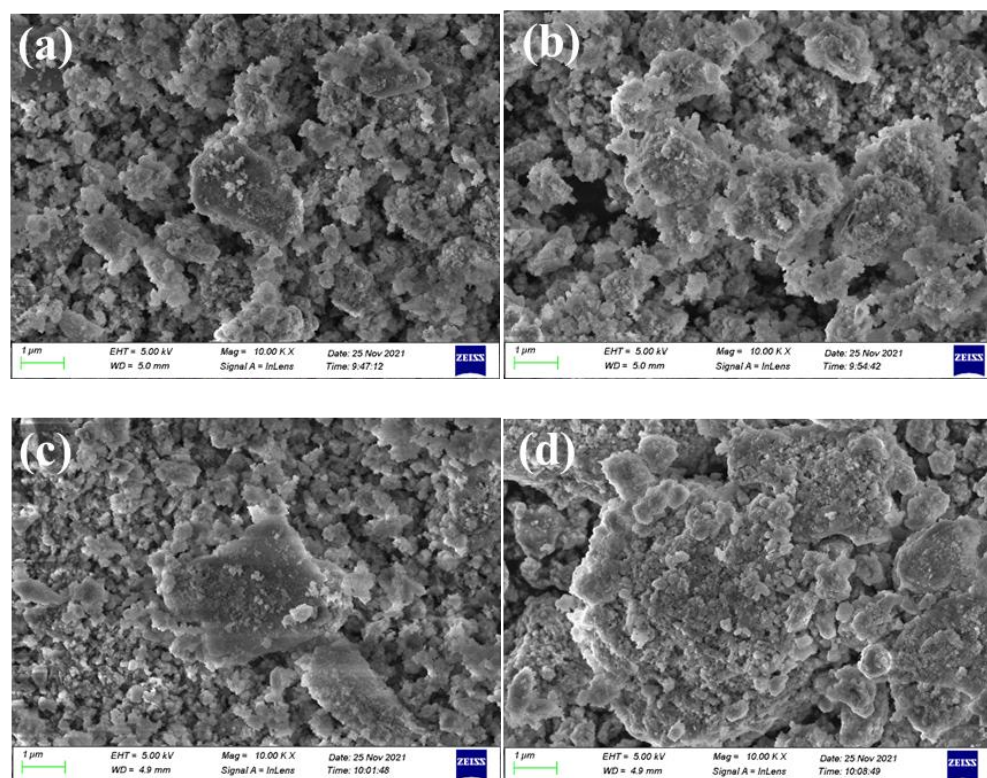


Figure 8. 10 K SEM image of desulfurized red mud. ((a) raw red mud desulfurization; (b) ball mill red mud desulfurization; (c) desulfurization of raw red mud under ultrasonication; (d) desulfurization of ball-milled red mud under ultrasonication).

3.3. Mechanism of Red Mud Desulfurization

As shown in Figure 9, the diffraction peaks of sodium aluminosilicate hydrate and calcium aluminosilicate hydrate mainly change during the desulfurization of red mud. In the initial stage of the reaction, hydrated sodium aluminosilicate first decomposes and dissolves aluminum and sodium. As the desulfurization reaction proceeds, the XRD diffraction peaks of both sodium aluminosilicate hydrate and calcium aluminosilicate hydrate gradually weaken. When desulfurization was carried out for 40 min, the pH was approximately four, and the phases of sodium aluminosilicate and calcium aluminosilicate hydrate were not observed in the desulfurized red mud. The raw red mud will have decomposed Al^{3+} combined with OH^- in the form of $\text{Al}(\text{OH})_3$ in the desulfurized red mud. Some of the Si is present as a stable structure of amorphous SiO_2 , which is also detected in the desulfurized red mud. After 20 min of reaction, CaCO_3 in the red mud decomposed, and the final desulfurized red mud did not contain Ca^{2+} , which was consistent with the XRF results in Table 2. Part of the hematite (Fe_2O_3) reacts with TiO_2 in a solid-state to form iron-titanium oxide ($\text{Fe}_2\text{Ti}_3\text{O}_9$). Finally, Fe exists in the form of Fe_2O_3 and $\text{Fe}_2\text{Ti}_3\text{O}_9$ in the desulfurized red mud.

Figure 10 shows the infrared spectra of the raw red mud desulfurization process. As shown in Figure 10, the main mid-infrared band that appears at $900\text{--}1000\text{ cm}^{-1}$ is the stretching vibration of the Si-O-Si bond [41]. The main mid-infrared band that appears at approximately 802 cm^{-1} is the bending vibration of the Si-O bond [42]. The reason is that as the desulfurization reaction proceeds, a large amount of Si in sodium aluminosilicate hydrate ($1.08\text{Na}_2\text{O} \cdot \text{Al}_2\text{O}_3 \cdot 1.68\text{SiO}_2 \cdot 1.8\text{H}_2\text{O}$) and hydrated garnet ($\text{CaO} \cdot \text{Al}_2\text{O}_3 \cdot \text{SiO}_2 \cdot 2\text{H}_2\text{O}$) dissolves in the aqueous solution, resulting in a weaker absorption band for the Si-O bond. The infrared band near 1410 cm^{-1} is the stretching vibration of the C-O-C bond in the CO_3^{2-} group of the red mud [43–45]. This is consistent with the XRD results, which prove the presence of CaCO_3 in the raw red mud. The IR peak gradually decreases to disappear,

and there is no CO_3^{2-} in the desulfurized red mud, indicating the participation of CaCO_3 in the desulfurization reaction. The infrared band at $1636\text{--}1640\text{ cm}^{-1}$ is the bending vibration of the H-OH bond. This indicates that there is more free water interacting with the reaction products to become bound water in the desulfurization process [46]. The infrared band at 2100 cm^{-1} is the stretching vibration of the Si-H bond. The broader infrared absorption band at 3140 cm^{-1} is the absorption peak of the interlayer molecule H_2O [47,48].

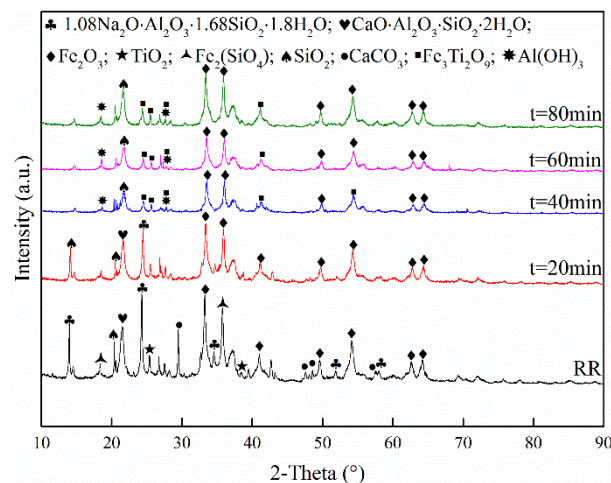


Figure 9. XRD of the raw red mud desulfurization process.

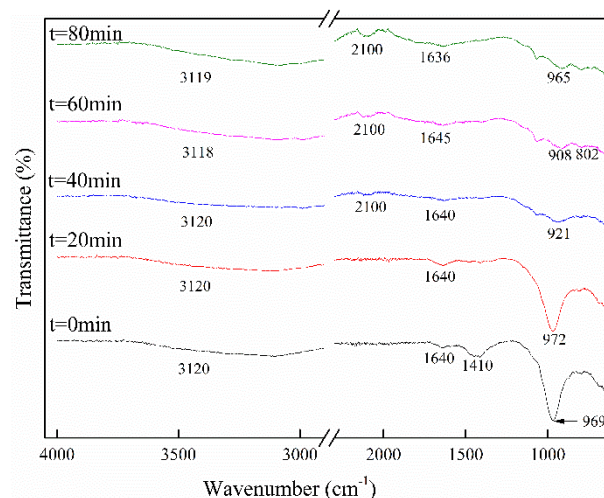


Figure 10. Infrared spectrum of the raw red mud desulfurization process.

In summary, the process of red mud slurry desulfurization is divided into three steps: (1) SO_2 gas is dissolved in the slurry. At this point, the dissolution of SO_2 in water to form H_2SO_3 and the ionization of H_2SO_3 to produce SO_3^{2-} and H^+ mainly occur. The unstable H_2SO_3 decomposes to produce HSO_3^- and H^+ . (2) The free alkali in the red mud slurry reacts with H^+ to neutralize it. Neutralization and oxidation reactions of alkaline metal compounds with H^+ also occur at this time. Al^{3+} metal ions combine with OH^- to generate precipitates. (3) Dissolution of insoluble sodium salts of red mud (sodium aluminosilicate hydrate, hydrated garnet) and the physical phase transfer of reaction products. The main reactions occurring in the red mud desulfurization process are shown in Equations (2)–(10), where OH^- is provided by the free base [33–36]. The dissolution of the red mud desulfurization process and the reaction mechanism are shown in Figure 11.



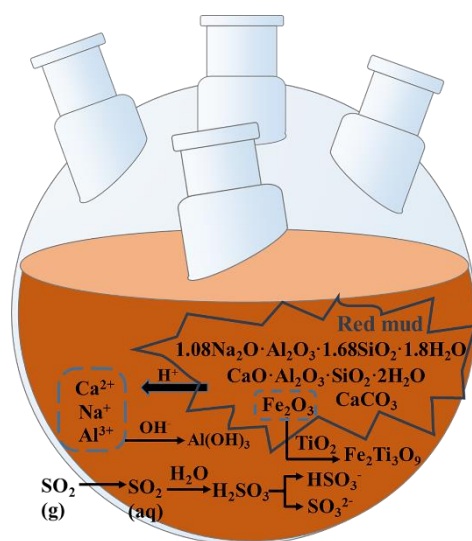
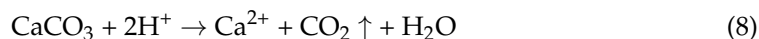


Figure 11. Mechanism of red mud desulfurization in the reactor.

4. Conclusions

In this study, the use of red mud desulfurization is an economic technology to treat waste with waste. It can not only solve the industrial flue gas SO_2 pollution problem but also reduce the stockpiling of red mud. Acid desulfurization slurry is recycled, and no waste acid is produced. In the bubbling and stirring reactor, the appropriate slurry concentration for red mud desulfurization is 10 g/L. The raw red mud can absorb 100% of SO_2 in the first 25 min, and the ability of red mud to absorb SO_2 decreases as the reaction time increases. Based on the result of 10 g/L raw red mud slurry desulfurization, 24.3 kg/m³ of red mud slurry is required to absorb 1 kg SO_2 . The red mud is mainly free alkali involved in the reaction at the beginning stage. Sodium aluminosilicate hydrate ($1.08 \text{ Na}_2\text{O} \cdot \text{Al}_2\text{O}_3 \cdot 1.68 \text{ SiO}_2 \cdot 1.8 \text{ H}_2\text{O}$), hydrated garnet ($\text{CaO} \cdot \text{Al}_2\text{O}_3 \cdot \text{SiO}_2 \cdot 2 \text{ H}_2\text{O}$), and CaCO_3 are dissolved in the liquid phase of the solid phase. Part of Fe_2O_3 reacts with TiO_2 in the solid phase to synthesize $\text{Fe}_2\text{Ti}_3\text{O}_9$. The metal oxides react with H^+ to form metal ions. Al^{3+} metal ions combine with OH^- to generate precipitates. Under the present experimental conditions, S is mainly present in the liquid phase after the reaction. After 60 min of red mud desulfurization, the Na_2O in red mud is <1%. This can meet the highly stringent requirements for the production of cement, geopolymers, etc. Under the external field of the ball mill, 100% SO_2 absorption can be achieved in 33 min, and under the external field of ultrasonic waves, 100% SO_2 absorption can only be achieved in 23 min. Therefore, comparing these two external field effects, it can be found that the ball mill external field is more suitable for improving the desulfurization rate in the bubbling and stirring reactor.

Author Contributions: Writing—original draft preparation X.L.; writing—review and editing, Y.L.; funding acquisition, Y.L. and T.Z. All authors have read and agreed to the published version of the manuscript.

Funding: This study was financially supported by the National Key R&D Program of China (grant numbers 2017YFC0210404 and 2017YFC0210403).

Data Availability Statement: Not applicable.

Conflicts of Interest: The authors declare no conflict of interest.

References

- Xue, S.G.; Kong, X.F.; Zhu, F.; Hartley, W.; Li, X.F.; Li, Y.E. Proposal for management and alkalinity transformation of bauxite residue in China. *Environ. Sci. Pollut. Res.* **2016**, *23*, 12822–12834. [\[CrossRef\]](#) [\[PubMed\]](#)
- Gu, H.; Hargreaves, J.S.J.; Jiang, J.Q.; Rico, J.L. Potential Routes to Obtain Value-Added Iron-Containing Compounds from Red Mud. *J. Sustain. Metall.* **2017**, *3*, 561–569. [\[CrossRef\]](#)
- Pei, J.N.; Pan, X.L.; Zhang, Y.M.; Yu, H.Y.; Tu, G.F. A novel process to fully utilize red mud based on low-calcium sintering. *J. Environ. Chem. Eng.* **2021**, *9*, 106754. [\[CrossRef\]](#)
- Power, G.; Grafe, M.; Klauber, C. Bauxite residue issues: I. Current management, disposal and storage practices. *Hydrometallurgy* **2011**, *108*, 33–45. [\[CrossRef\]](#)
- Zhu, X.B.; Li, W.; Guan, X.M. An active dealcalization of red mud with roasting and water leaching. *J. Hazard. Mater.* **2015**, *286*, 85–91. [\[CrossRef\]](#)
- Sanwani, E.; Jeremy, E.; Chaerun, S.K.; Mufakhir, F.R.; Astuti, W. Use of Mixotrophic Bacteria as Flocculating Agents to Separate Iron from Red Mud (Alumina Refinery Residue). *J. Sustain. Metall.* **2022**, *8*, 443–457. [\[CrossRef\]](#)
- Guo, T.F.; Yang, H.Q.; Liu, Q.; Gu, H.N.; Wang, N.; Yu, W.B. Adsorptive removal of phosphate from aqueous solutions using different types of red mud. *Water Sci. Technol.* **2018**, *2017*, 570–577. [\[CrossRef\]](#)
- Nadaroglu, H.; Kalkan, E.; Demir, N. Removal of copper from aqueous solution using red mud. *Desalination* **2010**, *251*, 90–95. [\[CrossRef\]](#)
- Smičiklas, I.; Smiljanić, S.; Perić-Grujić, A.; Šljivić-Ivanovića, M.; Mitrića, M.; Antonović, D. Effect of acid treatment on red mud properties with implications on Ni(II) sorption and stability. *Chem. Eng. J.* **2014**, *242*, 27–35. [\[CrossRef\]](#)
- Liu, W.C.; Sun, S.Y.; Zhang, L.; Jahanshahi, S.; Yang, J.K. Experimental and simulative study on phase transformation in Bayer red mud soda-lime roasting system and recovery of Al, Na and Fe. *Miner. Eng.* **2012**, *39*, 213–218. [\[CrossRef\]](#)
- Ochsenkühn-Petropoulou, M.T.; Hatzilyberis, K.S.; Mendrinou, L.N.; Salmas, C.E. Pilot-Plant Investigation of the Leaching Process for the Recovery of Scandium from Red Mud. *Ind. Eng. Chem. Res.* **2002**, *41*, 5794–5801. [\[CrossRef\]](#)
- Lockwood, C.L.; Mortimer, R.J.G.; Stewart, D.I.; Mayes, W.M.; Peacock, C.L.; Polya, D.A.; Lythgoe, P.R.; Lehoux, A.P.; Gruiz, K.; Burke, I.T. Mobilisation of arsenic from bauxite residue (red mud) affected soils: Effect of pH and redox conditions. *Appl. Geochem.* **2014**, *51*, 268–277. [\[CrossRef\]](#)
- Hua, Y.M.; Heal, K.V.; Hanl, W.F. The use of red mud as an immobiliser for metal/metalloid-contaminated soil: A review. *J. Hazard. Mater.* **2016**, *325*, 17–30. [\[CrossRef\]](#) [\[PubMed\]](#)
- Feigl, V.; Anton, A.; Uzniger, N.; Gruiz, K. Red Mud as a Chemical Stabilizer for Soil Contaminated with Toxic Metals. *Water Air Soil Poll.* **2012**, *223*, 1237–1247. [\[CrossRef\]](#)
- Gray, C.W.; Dunham, S.J.; Dennis, P.G.; Zhao, F.J.; McGrath, S.P. Field evaluation of in situ remediation of a heavy metal contaminated soil using lime and red-mud. *Environ. Pollut.* **2006**, *142*, 530–539. [\[CrossRef\]](#) [\[PubMed\]](#)
- Sglavo, V.M.; Maurina, S.; Conci, A.; Salviati, A.; Carturan, G.; Cocco, G. Bauxite ‘red mud’ in the ceramic industry. Part 2: Production of clay-based ceramics. *J. Eur. Ceram. Soc.* **2000**, *20*, 245–252. [\[CrossRef\]](#)
- Yalcin, N.; Sevinç, V. Utilization of bauxite waste in ceramic glazes. *Ceram. Int.* **2000**, *26*, 485–493. [\[CrossRef\]](#)
- Akın, A.; Artir, R. Characterization of trace elements and radionuclides and their risk assessment in red mud. *Mater. Charact.* **2008**, *59*, 417–421. [\[CrossRef\]](#)
- Piskin, S.; Figen, A.K.; Ozkan, E.; Ozcay, ü. Structural Characterization of Seydiehir Red Mud to Utilization in Roof Tile Manufacturing. *IFAC Proc. Vol.* **2013**, *46*, 484–487. [\[CrossRef\]](#)
- Tsakiridis, P.E.; Agatzini-Leonardou, S.; Oustadakis, P. Red mud addition in the raw meal for the production of Portland cement clinker. *J. Hazard. Mater.* **2004**, *116*, 103–110. [\[CrossRef\]](#)
- Li, Y.C.; Min, X.B.; Ke, Y.; Liu, D.G.; Tang, C.J. Preparation of red mud-based geopolymer materials from MSWI fly ash and red mud by mechanical activation. *Waste Manag.* **2019**, *83*, 202–208. [\[CrossRef\]](#) [\[PubMed\]](#)
- Yadav, V.S.; Prasad, M.; Khan, J.; Amritpale, S.S.; Singh, M.; Raju, C.B. Sequestration of carbon dioxide (CO₂) using red mud. *J. Hazard. Mater.* **2010**, *176*, 1044–1050. [\[PubMed\]](#)
- Xiao, K.K.; Guan, R.N.; Yang, J.K.; Li, H.S.; Yu, Z.C.; Liang, S.; Yu, W.B.; Hu, J.P.; Hou, H.J.; Liu, B.C. Effects of red mud on emission control of NO_x precursors during sludge pyrolysis: A protein model compound study. *Waste Manag.* **2019**, *85*, 452–463. [\[CrossRef\]](#) [\[PubMed\]](#)

24. Apeksha, M.; Rajanikanth, B.S. Plasma/adsorbent system for NO_x treatment in diesel exhaust: A case study on solid industrial wastes. *Int. J. Environ. Sci. Technol.* **2018**, *16*, 2973–2988. [\[CrossRef\]](#)
25. Sahu, R.C.; Patel, R.; Ray, B.C. Removal of hydrogen sulfide using red mud at ambient conditions. *Fuel Proc. Technol.* **2011**, *92*, 1587–1592. [\[CrossRef\]](#)
26. Nath, H.; Sahoo, A. Red Mud and Its Applicability in Fluoride Abatement. *Mater. Today Proc.* **2018**, *5*, 2207–2215. [\[CrossRef\]](#)
27. Yan, J.; Lu, X.F.; Sun, R.Y.; Zheng, X. An experimental study on the feasibility of in-situ desulfurization performance in a CFB combustor co-burning red mud and coal. *Fuel Proc. Technol.* **2021**, *223*, 106985. [\[CrossRef\]](#)
28. Liu, H.T.; Han, K.H.; Niu, S.L.; Lu, C.M.; Liu, M.Q.; Li, H. Experimental Study and Mechanism Analysis of Modified Limestone by Red Mud for Improving Desulfurization. In Proceedings of the International Symposium on Coal Combustion, Harbin, China, 17–21 July 2011; Springer: Berlin/Heidelberg, Germany, 2011; pp. 465–477.
29. Niu, J.; Zhang, H.R.; Li, L.B.; Guo, Y.X. Cost-effective activated carbon (AC) production from partial substitution of coal with red mud (RM) as additive for SO₂ and NO_x abatement at low temperature. *Fuel* **2021**, *293*, 120448. [\[CrossRef\]](#)
30. Wang, X.K.; Zhang, Y.H.; Lv, F.Z.; An, Q.; Lu, R.; Hu, P.; Jiang, S. Removal of alkali in the red mud by SO₂ and simulated flue gas under mild conditions. *Environ. Prog. Sustain.* **2014**, *34*, 81–87. [\[CrossRef\]](#)
31. Wei, P. Research of Industrial Flue Gas Desulfurization by Alumina Red Mud. Master's Thesis, Zhengzhou University, Zhengzhou, China, 2012.
32. Yang, J.J. Experimental Study of Red Mud for Industrial Flue Gas Desulfurization. Master's Thesis, Zhengzhou University, Zhengzhou, China, 2012.
33. Li, B.; Wu, H.; Liu, X.L.; Zhu, T.Y.; Liu, F.G.; Zhao, X.T. Simultaneous removal of SO₂ and NO using a novel method with red mud as absorbent combined with O₃ oxidation. *J. Hazard. Mater.* **2020**, *392*, 12270.
34. Tao, L.; Wu, H.; Wang, J.; Li, B.; Wang, X.Q.; Ning, P. Removal of SO₂ from flue gas using bayer red mud: Influence factors and mechanism. *J. Cent. South Univ.* **2019**, *26*, 467–478. [\[CrossRef\]](#)
35. Liu, Y.; Li, B.; Lei, X.L.; Liu, S.; Zhu, H.X.; Ding, E.; Ning, P. Novel method for high-performance simultaneous removal of NO_x and SO₂ by coupling yellow phosphorus emulsion with red mud. *Chem. Eng. J.* **2022**, *428*, 131991. [\[CrossRef\]](#)
36. Zhang, Y.W.; Qian, W.M.; Zhou, P.X.; Liu, Y.; Lei, X.L.; Li, B.; Ning, P. Research on red mud-limestone modified desulfurization mechanism and engineering application. *Sep. Purif. Technol.* **2021**, *272*, 118867. [\[CrossRef\]](#)
37. Sing, K.S.W. Reporting physisorption data for gas/solid systems with special reference to the determination of surface area and porosity (Recommendations 1984). *Pure Appl. Chem.* **1990**, *57*, 603–619. [\[CrossRef\]](#)
38. Nie, Q.K.; Hu, W.; Huang, B.S.; Shu, X.; He, Q. Synergistic utilization of red mud for flue-gas desulfurization and fly ash-based geopolymer preparation. *J. Hazard. Mater.* **2019**, *369*, 503–511. [\[CrossRef\]](#)
39. Agrawal, S.; Dhawan, N. Microwave acid baking of red mud for extraction of titanium and scandium values. *Hydrometallurgy* **2021**, *204*, 105704. [\[CrossRef\]](#)
40. Wang, Y.X.; Zhang, T.A.; Lyu, G.Z.; Guo, F.F.; Zhang, W.G.; Zhang, Y.H. Recovery of alkali and alumina from bauxite residue (red mud) and complete reuse of the treated residue. *J. Clean. Prod.* **2018**, *188*, 456–465. [\[CrossRef\]](#)
41. Lipinska-Kalita, K.E. Infrared spectroscopic investigation of structure and crystallization of aluminosilicate glasses. *J. Non-Cryst. Solids* **1990**, *119*, 310–317. [\[CrossRef\]](#)
42. He, L.N. Plasma-enhanced chemical vapor deposition amorphous SiO_x:H (0 ≤ x ≤ 2.0) films by infrared absorption spectroscopy. *Chin. J. Semicond.* **2001**, *22*, 587–593.
43. Lodeiro, G.; Fernández-Jiménez, A.; Blanco, M.T.; Palomo, A. FTIR study of the sol–gel synthesis of cementitious gels: C–S–H and N–A–S–H. *J. Solgel. Sci. Technol.* **2008**, *45*, 63–72. [\[CrossRef\]](#)
44. Shi, Z.G.; Shi, C.J.; Wan, S.; Li, N.; Zhang, Z.H. Effect of alkali dosage and silicate modulus on carbonation of alkali-activated slag mortars. *Cem. Concr. Res.* **2018**, *113*, 55–64. [\[CrossRef\]](#)
45. Miecznik, J.B.; Haberko, J.P.; Haberko, K.; Sitarz, W.; Mozgawa, M. The effect of NaOH and KOH treatment on the behavior of CO₃^{2−} and OH[−] groups in natural origin hydroxyapatite. *Ceram. Int.* **2017**, *43*, 12540–12545. [\[CrossRef\]](#)
46. Yu, P.; Kirkpatrick, R.J.; Poe, B.; McMillan, P.F.; Cong, X.D. Structure of Calcium Silicate Hydrate (C–S–H): Near-, Mid-, and Far-Infrared Spectroscopy. *J. Am. Ceram. Soc.* **1999**, *82*, 742–748. [\[CrossRef\]](#)
47. Maley, N.; Szafranek, I.; Mandrell, L.; Katiyar, M.; Abelson, J.R.; Thornton, J.A. Infrared reflectance spectroscopy of very thin films of a-SiH. *J. Non-Cryst. Solids* **1989**, *114*, 163–165. [\[CrossRef\]](#)
48. Chen, Y.F. Association of 2100 cm^{−1} infrared spectra with microstructure in hydrogenated amorphous silicon. *Solid State Commun.* **1989**, *71*, 1127–1130. [\[CrossRef\]](#)